
(This is a sample cover image for this issue. The actual cover is not yet available at this time.)

Journal of Manufacturing Processes 54 (2020) 28–37

Contents lists available at ScienceDirect

Journal of Manufacturing Processes

journal homepage: www.elsevier.com/locate/manpro

# Nanosecond pulsed laser processing turns engineering metal alloys antireflective and superwicking

Avik Samanta[a], Qinghua Wang[a], Gurjap Singh[a], Scott K. Shaw[b], Fatima Toor[c], Albert Ratner[a], Hongtao Ding[a,*]

[a] Department of Mechanical Engineering, University of Iowa, Iowa City, IA 52242, USA
[b] Department of Chemistry, University of Iowa, Iowa City, IA 52242, USA
[c] Department of Electrical & Computer Engineering, University of Iowa, Iowa City, IA 52242, USA

ARTICLE INFO

*Keywords:*
Superwicking
Superhydrophilic
Laser texturing
Antireflective
Metal alloys
Capillary

ABSTRACT

In this work, superwicking and antireflective properties are achieved on engineering metal surfaces by creating a surface pattern using a high energy nanosecond pulsed laser followed by a chemical immersion treatment. The high-energy nanosecond pulse laser scans the metal surface in air. Subsequently, the laser-textured surface is further treated by immersion in a 3-cyanopropyltricholosilane reagent. As a result of these two processes, microgrooves with micro- and nano-scale surface features are generated on the metal surface. Due to the created surface structure and favorable surface chemistry, water sprints uphill defying the gravity. The fast self-propelling movement of water is due to the supercapillary effect of the surface microchannel and the superhydrophilic surface nitrile group. The wicking effect on the processed surface follows the classical square root of time dependence. The processed surface shows good antireflective properties in the visible and infrared spectrum. Surface features, surface chemistry, wettability, surface reflectivity and wicking behavior are measured on AA6061 and Ti-6Al-4V specimens through Scanning Electron Microscopy (SEM), X-ray Photoelectron Spectroscopy (XPS), contact angle goniometer, UV-VIS-NIR spectrometer and high-speed camera, respectively.

## 1. Introduction

The wettability condition of a solid surface determines the behavior of liquids when they encounter each other. It plays a critical role in a wide range of applications such as biomedicine and dental treatment [1–3], fuel cells [4], microfluidics [5], and catalysts [6]. In general, the wetting of a solid surface by a liquid depends on three major factors [7]: (a) surface tension of the liquid, (b) the surface topography of the solid and (c) the surface chemistry of the solid. To achieve desired wettability condition for a solid surface, a specific combination of surface topography and surface chemistry is required.

Topography of a solid surface plays as one of the most influential roles to decide the wetting properties of the solid. Alteration of the surface wetting behavior of solids through surface topography change by nano-/micro-structuring has been studied in recent years [8–12]. Traditionally, surface textures for altering the wetting properties are prepared using different surface processing methods, i.e., photolithography [12], plasma techniques [13], wet chemical etching [14], and electron beam lithography [15]. In recent years, laser-based surface texturing emerged as a popular approach for surface nano-/micro-structuring for altering the surface wetting properties [16–19]. As the laser-based methods can process complicated shapes for a wide range of materials including metals, glasses, semiconductors, and polymers with ease of automation, it is well suited for surface texturing.

Traditionally, researchers in laser material processing used laser-induced periodic surface structure (LIPSS) consisting of laser-induced surface ripples with a periodicity equal or smaller than the wavelength of the laser radiation (much smaller than the effective laser spot size) to prepare hydrophilic surface. This approach does not use any additional chemical treatment after laser texturing. The treated specimens with LIPSS by femtosecond laser exhibit a hydrophilic behavior with a water contact angle ($\theta_w$) of 24°~76° on Ti-6Al-4V [18,20,21] immediately after laser treatment. They exhibited very stable superhydrophilicity for over 30 days [21]. As mentioned earlier, one of the major factors that influence surface wettability is surface energy which is affected by surface chemistry. Normally the higher the surface energy, the easier it is for the surface to get wetted. As laser processing of metal in air is a high energy processing and generates high temperature locally. As a result, textured metal reacts with atmospheric oxygen and generates metal oxide on the textured surface. Metal oxides are typically

* Corresponding author.
*E-mail address:* hongtao-ding@uiowa.edu (H. Ding).

https://doi.org/10.1016/j.jmapro.2020.02.029
Received 5 October 2019; Received in revised form 20 January 2020; Accepted 21 February 2020

hydrophilic because their electronic structure favors the formation of hydrogen bonds [22]. Metal oxides possess higher surface energy. For instance, immediately after laser treatment, the AA6061 surface contains $Al_2O_3$ and the aluminum atoms at the surface are electron deficient resulting in a formation of a hydrogen bond with interfacial water molecules. Therefore, the surfaces behave as superhydrophilic immediately after laser texturing. However, the $\theta_w$ started to increase with time and the surface wettability changes from hydrophilicity to hydrophobicity over time. Storage time and storage environment play a crucial role in the transition of wettability [23–25]. Immediately after laser texturing, these high energy surfaces transform into hydrophobic due to the adsorption of organic compounds from the surrounding atmosphere onto the oxide surface [24].

The term 'superwicking' is generally used for surfaces that possess an extreme affinity for a liquid so that liquid immediately spread on the surface as soon as they come in contact with each other. The $\theta_w$ is considered to be 0° for this kind of surface. Laser surface texturing of engineering metals is one of the approaches to achieve specific surface morphology that makes metal surface superwicking. Surface roughness plays a critical role in achieving desired wettability and capillary action over the surface [26]. In recent years, an expensive femtosecond laser nanotechnology has been employed by Vorobyev and Guo for making materials superwicking through surface nano-/micro-structuring [3,19,27,28]. They have applied this method for noble metals [19], silicon [28], glass [27] and human enamel and dentin surface [3] for consistent super wettability. They processed a superwicking surface on gold and platinum plates using femtosecond laser treatment [19]. They created parallel open microgrooves with porous nanostructures. The nanostructures consist of nanoprotrusions and nanocavities that were distributed on top of ridges and valleys of microgrooves. Their processed surface can transport methanol up to 24 mm vertically against gravity along the microgrooves at 1 cm/s speed. Later they used this process on silicon [28], glass [27] and human enamel and dentin surface [3] and water transported in a horizontal and vertical direction almost ~20 mm. However, processing surface with femtosecond laser is very expensive due to the high cost of femtosecond lasers. Demir et al. created holes on pure titanium foil by high-frequency nanosecond laser micro-drilling and removed the spatter by chemical etching by $H_2SO_4$ + HF aqueous solution. After that, anodic oxidation was performed to create a nanotubular $TiO_2$ layer, whose behavior switches between hydrophilic and hydrophobic once illuminated by UV light. Without UV light the surface was hydrophobic with $\theta_w$ ~140° and with UV light exposure, the surface was hydrophilic with $\theta_w$ ~20° [29].

The authors have developed a unique nHSN process using a nanosecond laser for metal alloys to achieve superhydrophobicity [30–34] and superhydrophilicity [31]. In this work, the nHSN process is further extended to achieve superwickability. To the authors' best knowledge, superwicking surface has never been produced by combining laser texturing and silane treatment. In this research an integrated laser-based process is demonstrated which combines laser texturing with nanosecond pulse laser followed by chemical immersion treatment with a hydrophilic silane reagent to achieve superwicking and antireflective surface. The novelty of this research lies in introducing water affinitive groups on top of laser-induced surface structure to achieve stable superhydrophilicity and superwickability. Open microchannels are created by nanosecond laser pulses and the textured surface is treated with hydrophilic silane to attach hydrophilic chemical group on top of microchannels. The article discusses the mechanism of attachment of hydrophilic chemical groups on the textured metal surface and the etching effect of the chemical immersion process to enhance the micro/nanostructure generation during the process. The superwicking behavior is captured with a high-speed camera on the vertical processed surface and the antireflectivity is measured by UV-VIS-NIR spectrometer and compared with an untreated surface. The surface chemistry and topography are also analyzed to describe the superwicking behavior of the processed surface. The superwicking behavior is measured in terms of the transport velocity of water against gravity on the processed surface.

## 2. Experiments

A nanosecond laser-based surface texturing process is developed for engineering metal alloys to achieve superwicking surfaces. This developed process consists of two steps: (1) nanosecond laser texturing in air (aNLT), during which a high energy nanosecond pulse laser with long pulse mode scans the material surface, (2) chemical immersion treatment (CIT), during which the laser textured surface is further chemically treated.

### 2.1. Nanosecond laser texturing with long pulse mode in air (aNLT)

The experimental setup for the nanosecond laser texturing tests uses a single-mode, long pulse Nd: YAG nanosecond laser (Spectra-Physics Quanta-Ray Lab-150, wavelength 1064 nm) with high pulse energy on the order of several hundreds of mJ/pulse. During the laser texturing process, the laser repetition rate is 10 pulses per second with a laser pulse duration of 120 ns. The size of the beam immediately after the laser source is ~20 mm. It has been directed to the scan head through a series of mirrors as shown in Fig. 1a and then focused on the sample. The intensity distribution is gaussian in nature. The average power was 0.95 W and the pulse energy was 95 mJ for each pulse. 100 μm spot size was used during the experiments. The process is performed at ambient conditions. The scanning speed was 1.25 mm/sec. A galvanometer laser scanner (SCANLAB intelliSCAN® 20) furnished with an f-theta objective with a focal length of 255 mm directs the laser to texture the top surface of the specimen. The specimen is kept in the air. The laser scan head scans the top surface of the work material in a zig-zag pattern. The X-spacing (or pitch) defines the distance between two sequential laser scan lines and is pre-set through computer control.

Fig. 1a shows the schematic representation of the nanosecond laser texturing system. The workpiece is kept on an XYZ table, which is positioned using computer-controlled stages. Fig. 1b shows the typical

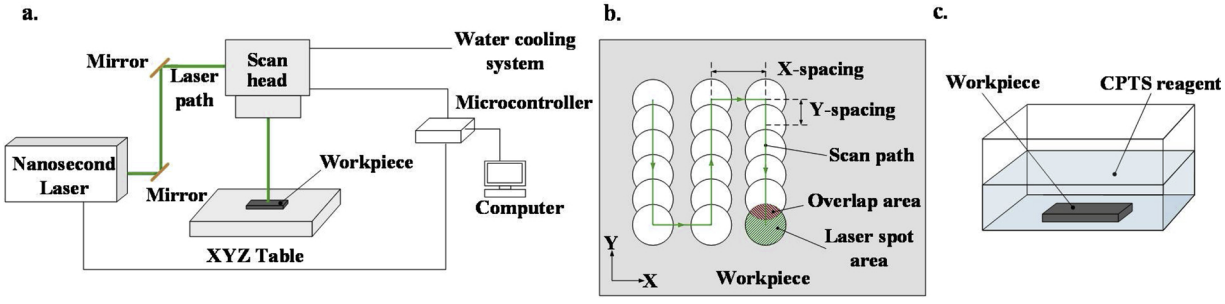


**Fig. 1.** Schematic representation of the process: (a) experimental setup of nanosecond laser texturing in the air; (b) laser scanning path; (c) experimental setup of chemical immersion treatment.

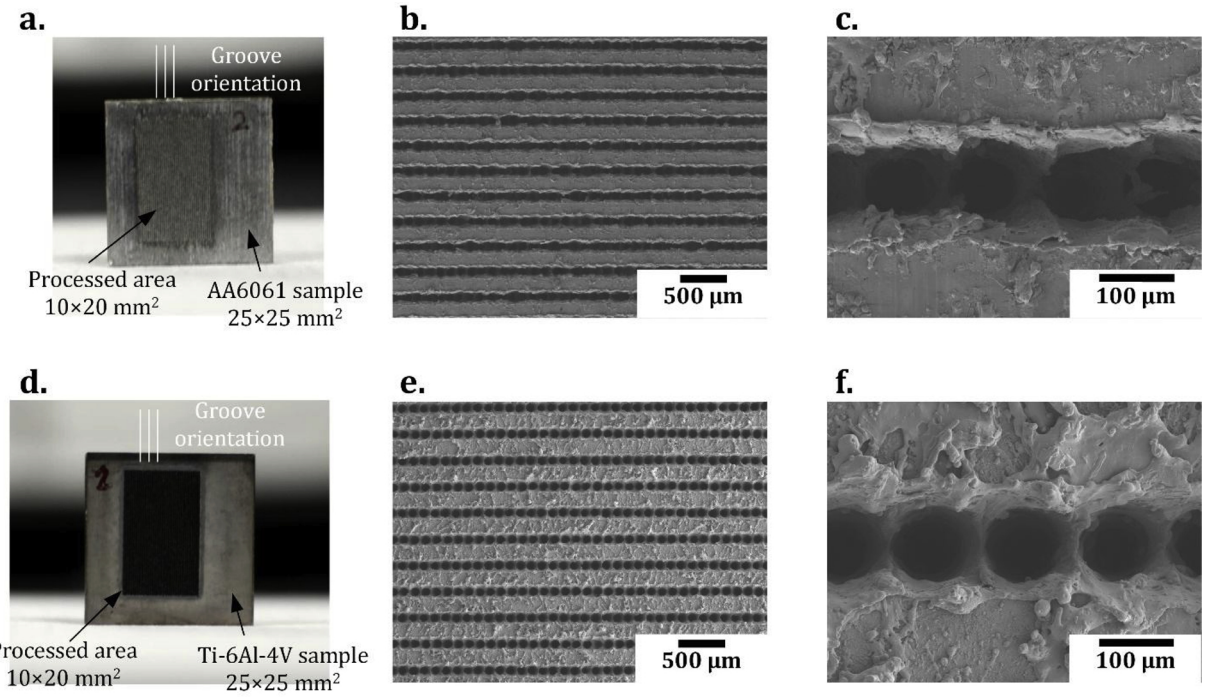


**Fig. 2.** Specimens processed with laser power intensity of 10 GW/cm$^2$: (a) a photograph of treated AA6061 sample; (b) SEM micrograph of microgrooves on AA6061; (c) close up SEM image of single microgroove on AA6061; (d) a photograph of treated Ti-6Al-4V sample; (e) SEM micrographs of microgrooves on Ti-6Al-4V; (f) close up SEM image of single microgroove on Ti-6Al-4V.

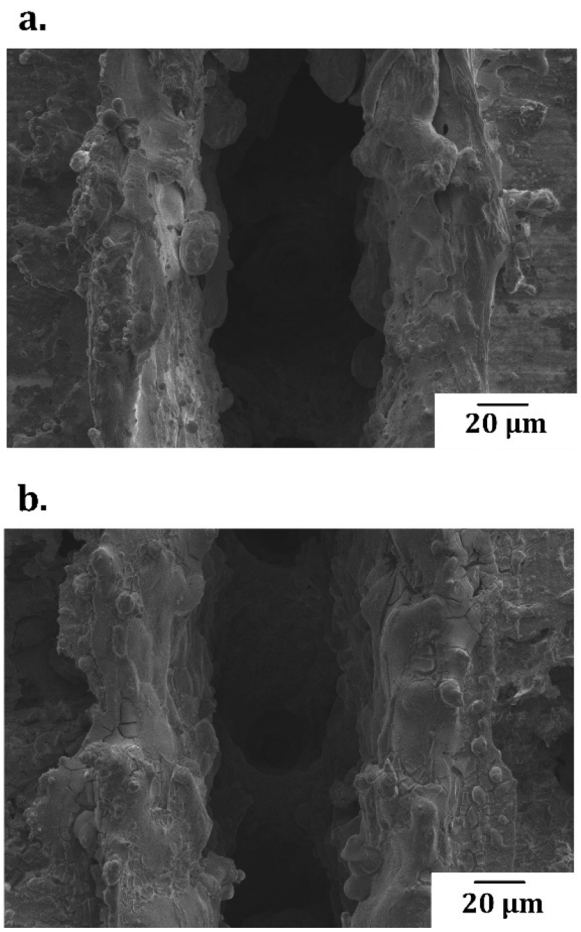


**Fig. 3.** Comparison of surface morphologies of the AA6061 between (a) only aNLT and (b) aNLT + CIT treatment.

laser scanning path used during the experiments. The laser scan head scans the top surface of the work material in a zig-zag pattern as shown in Fig. 1b. The X-spacing (or pitch) defines the distance between two sequential laser scan lines and is pre-set through computer control. The Y-spacing between two sequential laser shots along the scanning direction is determined by the laser repetition rate and pre-set laser scanning speed as shown in Eq. 1. The overlap ratio is set by the ratio of overlap area to the laser spot area as shown in Eq. 2. It is defined as the overlapped region between the two successive laser spots. Proper overlap ratio is selected to ensure the uniform width, depth and edge quality of the laser-textured microgrooves.

$$\text{Y-spacing} = \frac{\text{Laser Scanning Speed}}{\text{Laser Repetition Rate}} \quad (1)$$

$$\text{Overlap Ratio} = \frac{\text{Overlap Area}}{\text{Laser Spot Area}} \times 100\% \quad (2)$$

Both laser and scan head are controlled by a microcontroller for scanning along a pre-designed path. The scan head is also connected to a water-cooling system to avoid any undesirable heating of the scan head during the process.

### 2.2. Chemical immersion treatment (CIT)

After the laser texturing, the workpieces were immersed in an ethanol solution with 1.5 % volume percentage 3-cyanopropyltricholosilane reagent [$CN(CH_2)_3SiCl_3$], also known as CPTS at room temperature for ~3 h as shown in Fig. 1c. Workpieces were then cleaned with deionized water and dried using compressed air. Finally, it was kept at 80 °C in a vacuum oven for 1 h to dry it out completely.

### 2.3. Measurement and characterization

The surface morphology of the superwicking surface was analyzed using a Hitachi S-4800 scanning electron microscope (SEM). The SEM images were taken at 1.8–2.0 kV acceleration voltages. Surface profile

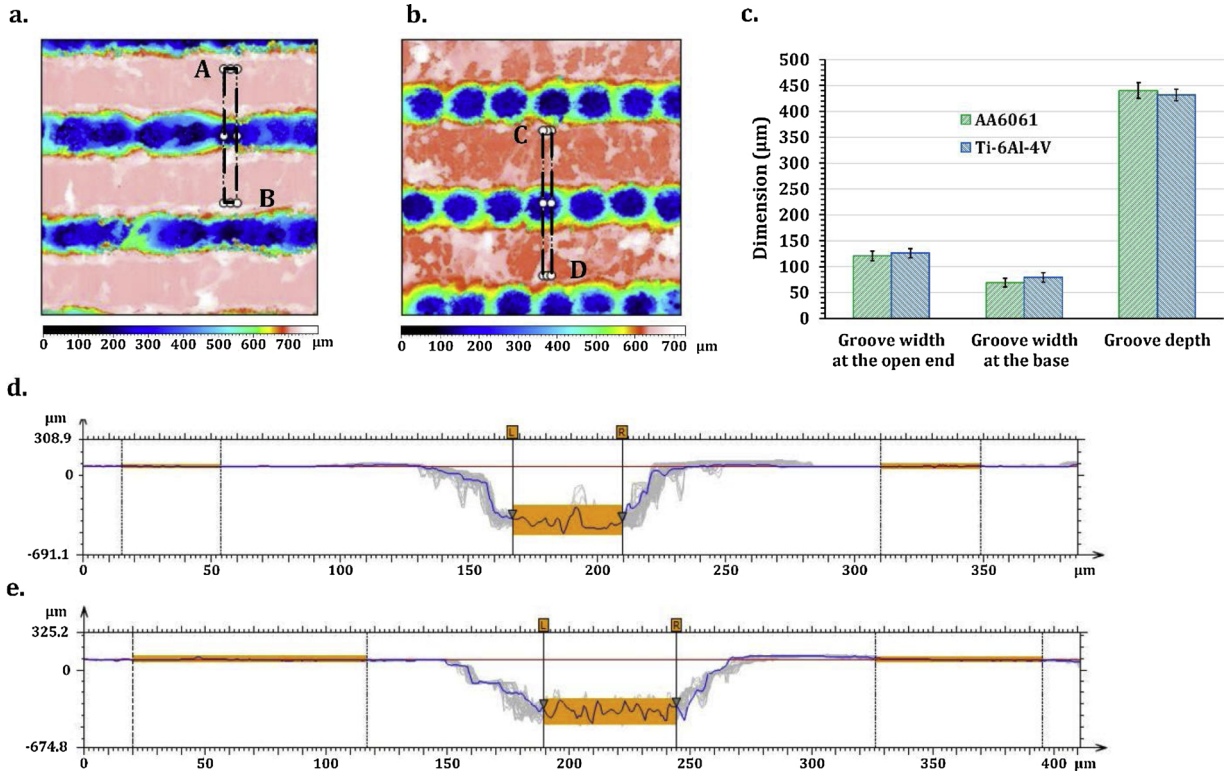


**Fig. 4.** Optical profile of the textured surface: (a) surface topography of the treated AA6061; (b) surface topography of the treated Ti-6Al-4V; (c) average groove width at the open and base side of the groove and groove depth on the treated surface; (d) cross-section of microgroove at location A-B in (a); and (e) cross-section of microgroove at location C-D in (b).

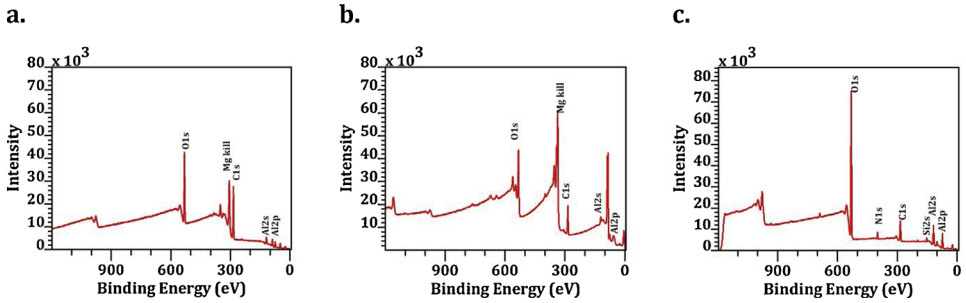


**Fig. 5.** XPS survey of the surface layer for (a) untreated AA6061 specimen; (b) specimen underwent laser texturing, and (c) specimen underwent both laser texturing and subsequent chemical immersion treatment with CPTS silane reagent.

of the treated sample was examined by a non-contact compact confocal microscope from Mahr (MarSurf CM Explorer with 1.4 M P 16-bit HDR camera). Additionally, X-ray photoelectron spectroscopy (XPS) analysis was carried out for the surface chemistry using a Kratos Axis Ultra high-performance XPS system. For the untreated sample, the XPS analysis was performed on the surface whereas for the laser-treated and laser + chemical treated, it is carried on the bottom surface of the micro-grooves. Full survey spectra and high-resolution elemental spectra were acquired for surface composition analysis and chemical state identification, respectively. $\theta_w$ for the treated specimen surface was measured during the wettability test using a contact angle goniometer (Rame-Hart model 100) coupled with a high-resolution CMOS camera (6 ~ 60× magnification, Thor Laboratories). For each $\theta_w$ measurement, about 5 µL volume of water was dropped to form a still water droplet on the specimen surface, and its optical shadowgraph was obtained using the CMOS camera. Multiple $\theta_w$ measurements were performed at various locations inside each specimen surface. The process of droplet wicking on the engineered superhydrophilic surface was captured using a black and white IDT X-StreamVision XS-3 CCD camera operated at 2250 frames/second and fitted with a 50 mm lens (Nikon AF Micro-Nikkor-F/1.4) to trace droplet evolution. The illumination of the processed surface was provided by an array of white LED lights. Three measurements were taken for each sample in the water wicking experiment and average water spreading height was presented. The spectral reflectance in the visible and infrared regions of the superwicking surfaces was characterized using a UV-VIS-NIR spectrometer (USB4000 & FlameNIR, Ocean Optics Co.). An integrating sphere was connected to the spectrometer for reflectance data collection. Before reflectance measurement, calibration of the reflectance scale was performed by measuring the incident flux remaining in the sphere after reflecting from standard reference material. Then the sample was placed against the entrance port for the actual reflectance measurement. Both specular reflection and diffuse reflection were taken into consideration for the measurement. OceanView® software was utilized to process and visualize the spectral reflectance measurement results. Each reflectance measurement was taken on a unit area of 1.13 $cm^2$ and four measurements were taken for each sample. The spectral reflectance measurement results were averaged and reported.

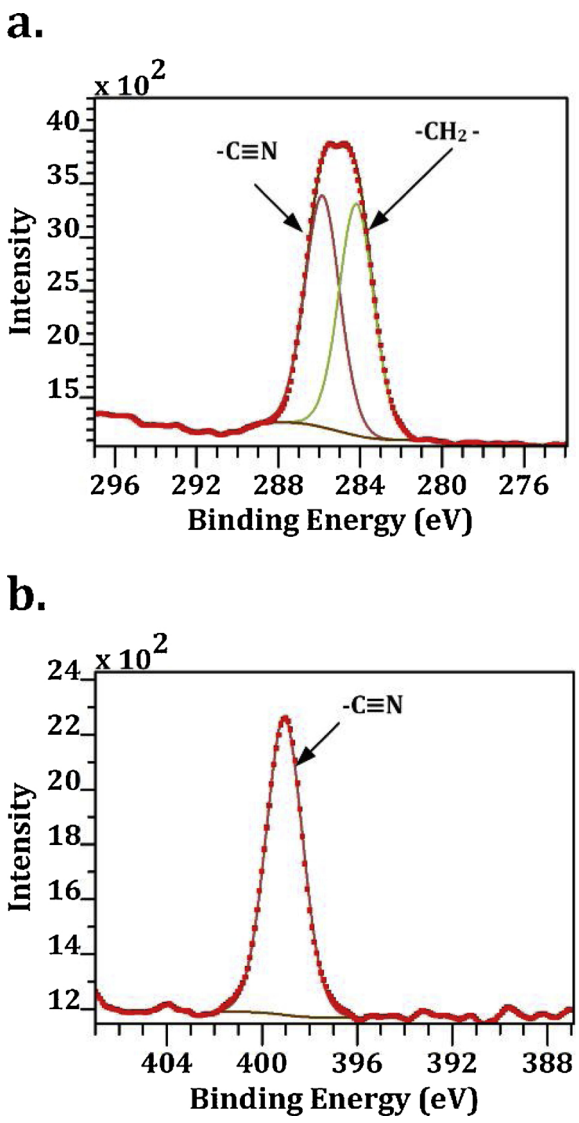


**Fig. 6.** Core level XPS analysis for (a) carbon and (b) nitrogen on the specimen that underwent both laser texturing and subsequent chemical immersion treatment with CPTS silane reagent.

## 3. Results and discussions

### 3.1. Surface microstructure and morphology

Photographs of the processed AA6061 and Ti-6Al-4V are shown in Fig. 2a and d. SEM images of the processed surface are provided in Fig. 2b-c and e–f for AA6061 and Ti-6Al-4V respectively. Fig. 2b and e show that the processed surface has multiple parallel microgrooves with a width of ~100 μm and a period of ~250 μm. SEM image with higher magnification shows that the microgrooves consist of a series of holes connected to form a microchannel. The ridges and valleys of the microgrooves are covered with nanostructures and microstructures. The nanostructures and microstructures on top of the microchannel are primarily caused by the melt expulsion. The chemical etching effect during the chemical immersion process also contributes to some extent for the nanostructure generation.

Higher magnification SEM micrographs show that the ridges and valleys of the micro-trenches were covered with random micro-/nano-structures after the aNLT process, as shown in Fig. 3a. Those micro-/nano-structures include randomly distributed burrs, ripples, protrusions, pores and cavities. This micro-/nano-structures formation is not suitable for conventional products, but it is helpful for super-wicking surfaces. They were deposited primarily due to melting, splashing and resolidification in sequence during laser-metal interaction. The presence of those random surface structures makes the treated surface amorphous which eventually increases the permeability of the surface. Higher permeability leads to increased capillary pressure resulting in better wicking effect [35]. Fig. 3b shows the higher magnification surface morphologies after the completion of both aNLT and CIT process. It can be clearly seen that the surface became more amorphous after the CIT process. There were more randomly distributed micro/nanopores on the wall and flat area of the treated surface. This indicated that the CIT process also influenced the surface morphology change.

To measure the surface profile of the microgrooves, confocal microscopy analysis was performed on the treated AA6061 and Ti-6Al-4V surface as shown in Fig. 4a and b. The topographs were sectioned at different locations along the groove to acquire the 2D cross-sectional profile as shown in Fig. 4d and f. Ten measurements of cross-section were taken along five microgrooves, and the average value was presented in Fig. 4c. The cross-sectional view of the microgrooves shows the existence of micro-scale peaks and valleys along the base of the microgrooves. The microgrooves had a wider width at the open side with an average value of 121 μm and 126 μm, for AA6061 and Ti-6Al-4V respectively. The micro-grooves had a relatively narrow width at the base side with an average value of 68 μm and 79 μm, respectively. The average depth of the microgrooves was 440 μm and 431 μm for AA6061 and Ti-6Al-4V respectively.

### 3.2. Surface chemistry

The elemental composition of the treated surface was investigated using the XPS survey analysis as shown in Fig. 5. It can be observed that untreated AA6061 specimen has oxygen, carbon, aluminum and magnesium on the surface as shown in Fig. 5a. The aluminum and magnesium came from the composition of AA6061 and oxygen came from the surface oxide layer. Carbon came from organic contamination on the untreated surface. Immediately after laser texturing, similar elements (oxygen, carbon, aluminum and magnesium) were detected on the laser textured surface. The XPS measurement is carried out at the bottom surface of the microgrooves which are 450 μm below the original surface. Usually the oxide layer thickness on untreated aluminum or aluminum alloy is several nanometers. So, it can be concluded that the oxide layer of the untreated sample was disrupted during the laser texturing and the new oxygen signal in XPS is coming from the oxidation that happened during laser texturing in the air. The aluminum and magnesium came from the composition of AA6061 (Fig. 5b). For the sample which went through both laser texturing and subsequent chemical immersion treatment, significantly different XPS spectra were observed. Two additional peaks in nitrogen and silicon along with oxygen, carbon, aluminum and magnesium were observed in the survey at the surface (Fig. 5c). The source of nitrogen and silicon belonged to CPTS silane reagent [$CN(CH_2)_3SiCl_3$]. Surprisingly, no chlorine signal was observed in the XPS survey though there is chlorine in the CPTS reagent. It is hypothesized that the chlorine elements in CPTS silane reagent reacted with metal oxide and dissolved in the chemical solution. Core level analysis for carbon and nitrogen elements was also carried out on the specimen that underwent both laser texturing and chemical immersion treatment. Core level analysis of carbon element shows the presence of –CN and $-CH_2$- at ~286 eV and ~284 eV respectively as shown in Fig. 6a. The presence of the –CN group can also be seen from the core level analysis of the N element as shown in Fig. 6b. This proves the presence of a nitrile group (R-C≡N) on the processed surface. –CN group is known to be highly polar due to the presence of highly electronegative nitrogen atom in the chemical structure.

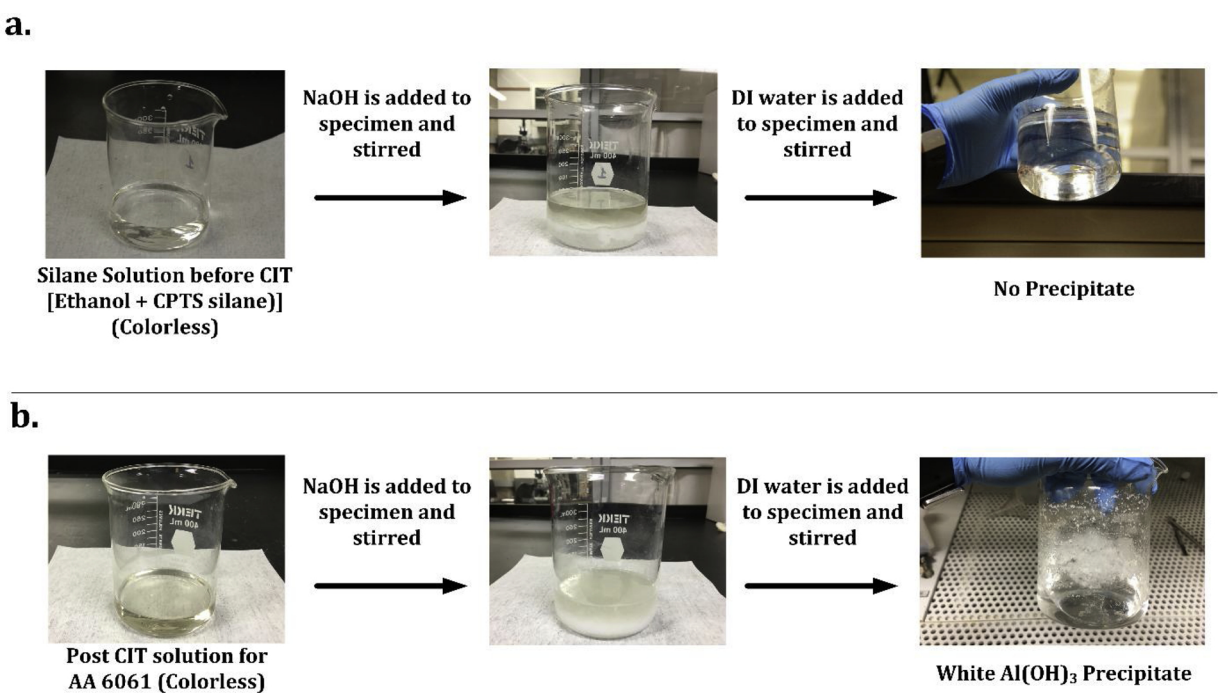


**Fig. 7.** Chemical analysis to show the etching effect by adding NaOH and DI water. (a) chemical analysis of silane solution before CIT showing no precipitate, and (b) chemical analysis of post CIT process solution showing white $Al(OH)_3$ precipitate.

As electronegativity of nitrogen is very high, it pulled the electrons in the triple covalent bond in the CN group towards itself. Nitriles, therefore, have strong permanent dipole-dipole attractions as well as van der Waals dispersion forces between their molecules [36–38]. Water is a polar molecule and it consists of a slightly positive hydrogen atom and a slightly negative −OH group. The positive hydrogen atom in a water molecule is attracted to the lone pair on the nitrogen atom in the nitrile group, and a hydrogen bond is formed. This makes the surface attracted to water and alcohol molecules that contribute to superhydrophilicity.

It can be observed from the XPS survey analysis, that there is no chlorine signal (198.5 ~ 200 eV) although there were three chlorine atoms in the chemical structure of the CPTS reagent $[CN(CH_2)_3SiCl_3]$. This is because the chlorine atoms must have reacted with the aluminum substrate during the CIT process and dissolved in the chemical solution as aluminum chloride [31]. After the chemical immersion treatment, post-process liquid solution was chemically tested to find out the etched away metal elements in the solution. Sodium hydroxide (NaOH) and deionized water were added to the solution. After some time, white precipitates were formed as shown in Fig. 7b. From the color of the precipitates, they are believed to be Aluminum Hydroxide $[Al(OH)_3]$. As $Al(OH)_3$ is insoluble in both water and ethanol, it is precipitated as white substance. The chemical reaction can be found in Eq. 3.

$$AlCl_3 + 3NaOH = Al(OH)_3 \downarrow + 3NaCl \quad (3)$$

On the other hand, when the same test was performed on the CPTS silane solution before the CIT process, no precipitate was found as shown in Fig. 7a. This proved that etching happened by the chlorine atoms of CPTS reagent during the chemical immersion treatment that brought Al elements from the substrate to the solution.

### 3.3. Static contact angle

The surface wettability is defined as the tendency of a liquid to spread on or adhere to a solid surface without the formation of droplets. The wettability of a surface to water is quantified using $\theta_w$ measurement. $\theta_w$ is defined as the angle, conventionally measured through the water droplet, where water–vapor interface meets a solid surface and can be used to quantify the wettability of a solid surface. The surface wettability to water can be categorized into four categories: hydrophobic, hydrophilic, superhydrophobic and superhydrophilic. When the $\theta_w$ is greater than 150°, the surface is generally regarded as superhydrophobic. Surfaces with $150° < \theta_w < 90°$ are categorized as hydrophobic. If the $\theta_w$ is between 10° and 90°, the surface is designated as hydrophilic. If $\theta_w$ is less than 10°, the surface is designated as superhydrophilic, and the water completely spreads over the surface. If the $\theta_w$ is equal to 0°, the surface is categorized as a highly superhydrophilic or superwicking surface.

To study the static wetting behavior of the processed surface for both AA6061 and Ti-6Al-4V, the processed sample is placed on the horizontal surface with the grooves orientation is in the Y direction as shown in Fig. 9. A water droplet of 5 μl is slowly brought in contact with the surface and the water-droplet spreading is captured at 15 frames per second. The untreated and only chemically treated AA6061 surface has a $\theta_w$ of 92° ± 0.5° and 87° ± 0.8° respectively. The wettability condition of the laser textured surface without chemical treatment is very unstable. The laser textured surface without chemical treatment shows superhydrophilicity immediately after laser treatment with $\theta_w < 10°$. However, the wettability is unstable and changes with time as shown in Fig. 8. Within 30 days, the surface wettability undergoes a transition from superhydrophilicity to superhydrophobicity. The $\theta_w$ becomes ~150° after 30 days due to a change in the chemistry of the surface [23,24]. The wettability conditions change due to the adsorption of organic compounds from the surrounding atmosphere onto the only laser textured surface [24]. For the laser textured surface with chemical treatment, the wettability has been monitored for 30 days. It shows a steady superhydrophilicity, and the $\theta_w$ remained at 0° over the experiment time as shown in Fig. 8.

This is a special case of the superhydrophilic surface where the liquid spread on the surface at a very high speed when the liquid droplet comes in contact with the surface. Fig. 9a and b show the different frames of the progress of the spontaneous wetting of the processed AA6061 and Ti-6Al-4V surfaces that undergoes both laser texturing and

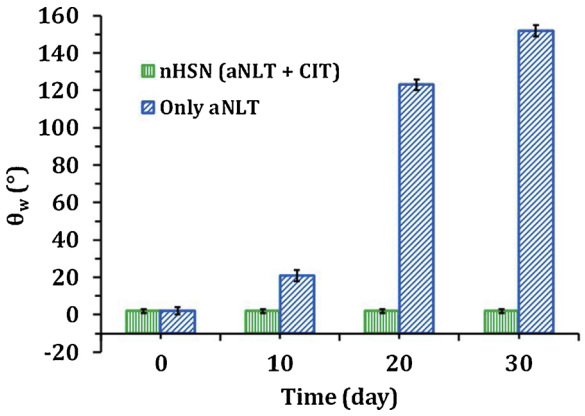


**Fig. 8.** Change of wettability of only aNLT and aNLT + CIT treated AA6061 surface.

chemical treatment. Frame 1 stands for the position of the 5 µl water droplet at the beginning. Frame 2 stands for the position of the water droplet just before it touches the surface. Frame 3 shows the onset of water spreading on the surface and frame 4 shows the surface immediately after the water spreading. As soon as the water droplet touches the surface, the processed surface draws the water molecules towards it and spread on the surface immediately. This proves that the processed surface is highly superhydrophilic or superwicking.

### 3.4. Water spreading on a vertical surface

The surface wetting properties of the processed AA6061 and Ti-6Al-4V are further studied by capturing the water spreading on the vertical surface. The specimen is positioned vertically with the grooves oriented as shown in Fig. 10a. An LED light is used to illuminate the processed surface. A distilled water droplet with 10 µl volume is introduced to the bottom of the grooves. The water-spreading dynamics is recorded by a black, and white IDT X-StreamVision XS-3 CCD camera operated at 2250 frames/second.

As shown in Fig. 11a, a 10 µl water droplet is pipetted at the bottom of the microgrooves, and the progress of the waterfront is captured by CCD camera. We can see that the water drop spreads highly anisotropically on the processed area and it flows preferentially along the microgrooves. Within 300 ms, the waterfront moves almost ~15 mm vertically against gravity with an average velocity of approximately 5 cm/s. For the Ti-6Al-4V sample, the water drop moves more anisotropically compared to the AA6061 sample as illustrated in Fig. 11b. It also moved a higher distance (~16.5 mm) compared to the AA6061 sample in the same time frame, thus attained an average vertical speed of 5.5 cm/s. The distance of water spreading front on the vertically-standing specimen is plotted against time$^{0.5}$ to determine the type of superwicking dynamics and shown in Fig. 10b. The spreading distance linearly depends on time$^{0.5}$ which indicates the capillary force is very strong in the processed surface and transforms the surface into superwicking.

The capillary effect inside a tube is a very familiar scientific phenomenon. It is also generated in an open half-tube or a channel. Hence, through fabricating a group of parallel microgrooves on a substrate surface, a strong capillary surface can be produced on a large area. Therefore, unidirectional microgrooves were deliberately fabricated in this work to let the water spread in one direction so that the wicking effect can be maximized in that direction. It is able to produce a superwicking surface where the water molecules were drawn at a very fast rate through the micro-trenches due to the capillary effect. However, the capillary force in a half-tube is less compare with a full tube [39]. The dynamics of liquid transport inside a vertical closed tube is defined by the Washburn equation, given by:

$$h(t) = \left(\frac{\gamma r \cos\theta}{2\mu}\right)^{0.5} * t^{0.5} = (Dt)^{0.5} \tag{4}$$

where $h(t)$ is the liquid transport distance in the vertical direction at time $t$, $\gamma$ stands for the surface tension of the liquid, $\mu$ is the liquid viscosity, $r$ is the capillary radius, $\theta$ is the contact angle and $D$ is the capillary performance parameter.

Wicking dynamics on open V-shaped open groove also follows Washburn-type dynamics [40] where wicking height is proportional to $t^{0.5}$. As shown in Fig. 4, the fabricated microgrooves were also open type and had a V-shape with flat bottom. Therefore, our experimentally measured data were expected to follow Washburn dynamics. Capillary radius ($r$) was calculated using the definition of hydraulic radius r = A/P from the capillary model [35], where A and P are the area and perimeter of the cross-section of the micro-trenches as shown in Fig. 4.

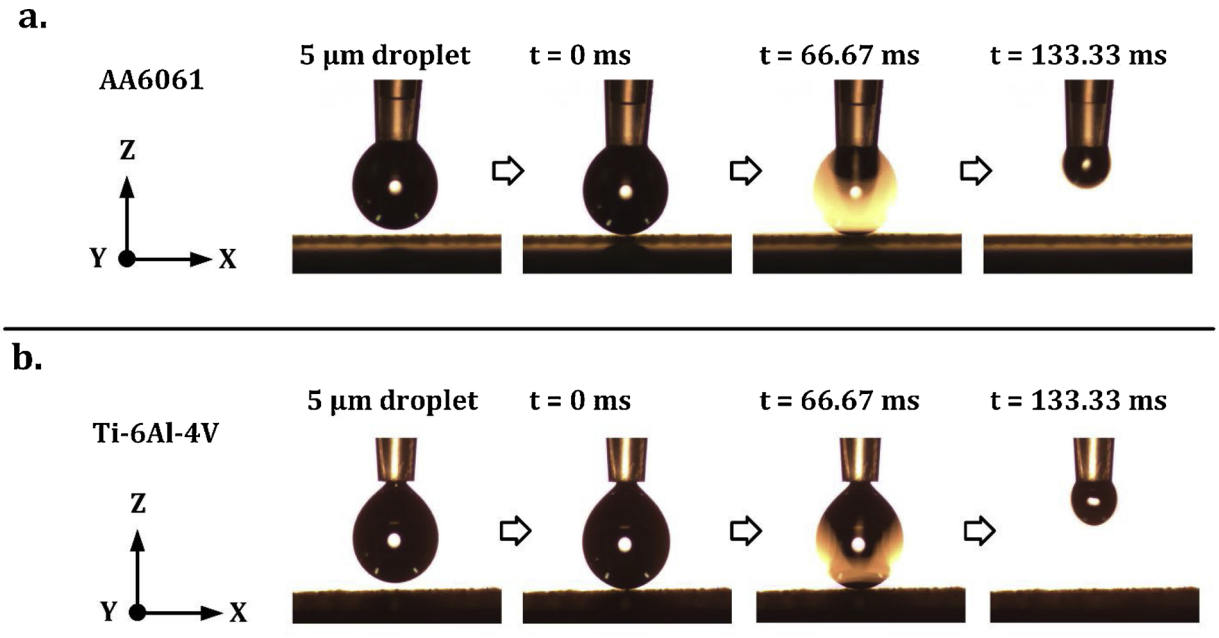


**Fig. 9.** Spontaneous wetting of the processed surface; (a) AA6061 and (b) Ti-6Al-4V.

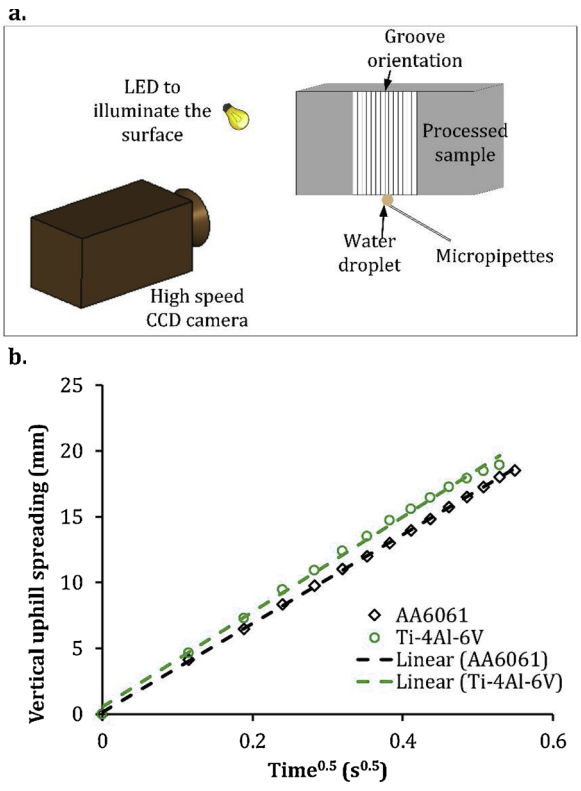


**Fig. 10.** Wicking distance measurement: (a) schematic of the high-speed camera setup to capture the spreading dynamic. (b) plot of the vertical uphill spreading distance of wetting front against time$^{0.5}$.

Previously, capillary driven liquid flow with Washburn dynamics has been observed on the vertically placed surface with open microgrooves [28], 2-D arrays of pillars [12], and under microgravity condition [41]. The dimension of the surface structures created in this study fell within the rage of the capillary size required for Washburn dynamics [42]. Fig. 10b shows that experimentally measured wicking height also follows Washburn dynamics for this study. Eq. 4 indicates that stronger capillary action is created when θ is smaller. Since the water affinitive nitrile surface chemistry was created in the capillary systems leading to intrinsic superhydrophilicity, the nHSN treated surface was expected to enhance the capillary action.

### 3.5. Reflectance in visible and infrared spectra

Spectral reflectance measurement results are shown in Fig. 12a for AA6061 specimens using various x-spacing from 250 μm to 350 μm. According to the classification by the International Commission on Illumination CIE, the electromagnetic spectrum between 400 ~ 3000 nm is subdivided into a visible spectrum from 450 nm to 700 nm, IR-A spectrum from 700 nm to 1400 nm, and IR-B spectrum from 1400 nm to 3000 nm. Following this classification, the spectrum of this reflectance measurement of 450 ~ 1670 nm is subdivided into a visible spectrum from 450 nm to 700 nm, IR-A spectrum from 700 nm to 1400 nm, and IR-B spectrum from 1400 nm to 1670 nm.

Spectral reflectance measurement results for untreated and mechanically ground AA6061 specimens are also shown for comparison. The spectral reflectance for the untreated AA6061 specimens falls ~55 % within the visible spectrum, 55 % ~ 76 % within the IR-A spectrum, 76 % ~ 87 % within the IR-B spectrum. The spectral reflectance for the mechanically ground AA6061 specimens falls ~66 % within the visible spectrum, 65 %–80 % within the IR-A spectrum, 80 %–84 % within the IR-B spectrum.

Using the x-spacing from 250 μm to 350 μm, the spectral reflectance of superwicking AA6061 specimens reduced to 13 % ~ 16 % within the visible spectrum, 13 %–21 % within the IR-A spectrum, 16 %–38 % within the IR-B spectrum. The lower the x-spacing is applied, the lower the surface spectral reflectance will be achieved for the superwicking AA6061 samples. Fig. 12b illustrates the spectral reflectance

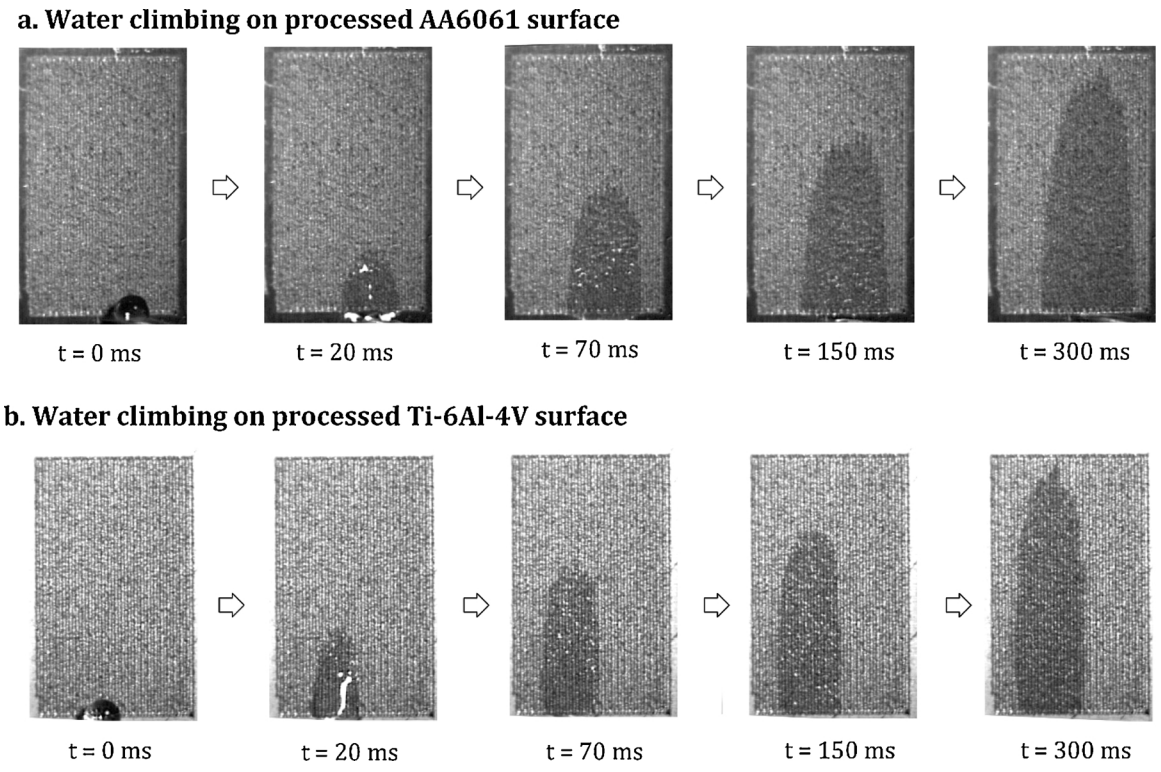


**Fig. 11.** High-speed images were taken at 2250 frames per second showing water running uphill against gravity on a vertically positioned sample: (a) progress of water moving uphill for AA6061 sample and (b) progress of water moving uphill for Ti-6Al-4V sample.

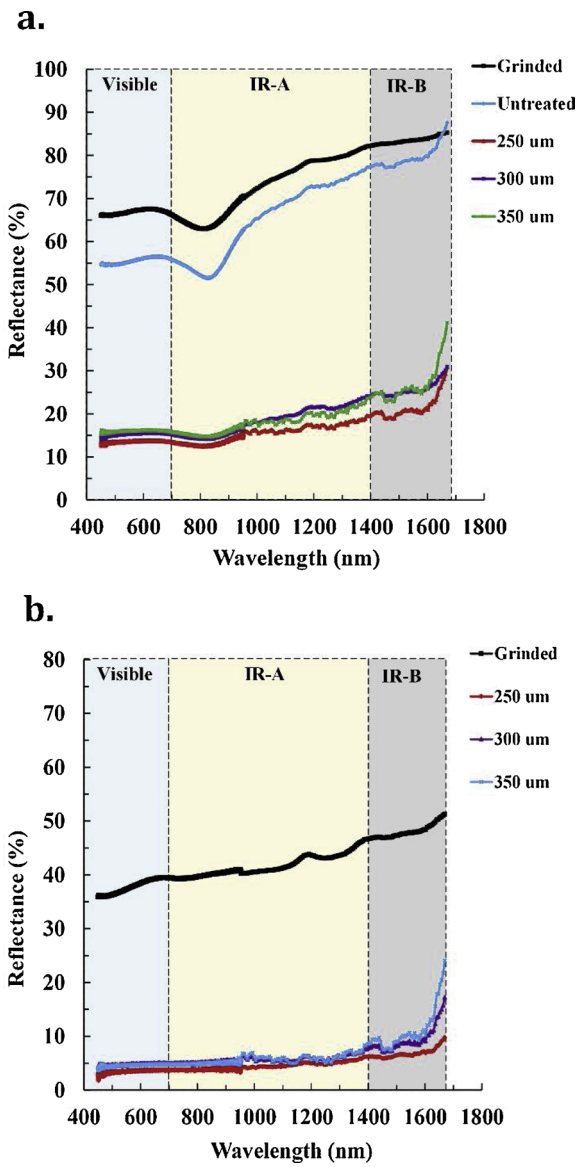


**Fig. 12.** Reflectance measurement for processed surface: (a) AA6061 and (b) Ti-4Al-6V.

measurement results for Ti-6Al-4V specimens. The spectral reflectance for the mechanically ground Ti-6Al-4V specimens falls 36 %∼40 % within the visible spectrum, 40 %–45 % within the IR-A spectrum, 45 %–51 % within the IR-B spectrum. Using the x-spacing from 250 μm to 350 μm, the spectral reflectance of superwicking Ti-6Al-4V specimens reduced to 3%∼5% within the visible spectrum, 3 %–5 % within the IR-A spectrum, 3 %–21 % within the IR-B spectrum.

## 4. Conclusions

A surface texturing process is developed that combines laser surface texturing and chemical immersion treatment in a silane solution to produce superwicking engineering metal surface. Due to superwicking capability, the processed surface pumps water vertically defying gravity. The super-capillary effect of the processed surface along with surface chemistry promotes the self-propelling high-speed vertical movement of water. The water-spreading dynamics follows the classical Washburn dynamics where the wicking height is proportional to the square root of transport time. The processed surface also shows good antireflective properties in the visible and infrared spectrum. Future work will extend the process for other engineering materials and optimize the surface microstructure to achieve better performance.

## Declaration of interests

The authors declare that they have no known competing financial interests or personal relationships that could have appeared to influence the work reported in this paper.

## Acknowledgments

The authors gratefully acknowledge the financial support by the National Science Foundation under Grant Number CMMI-1762353

## References

[1] Lampin M, Warocquier-Clérout R, Legris C, Degrange M, Sigot-Luizard MF. Correlation between substratum roughness and wettability, cell adhesion, and cell migration. J Biomed Mater Res 1997;36:99–108. doi:10.1002/(SICI)1097-4636(199707)36:1 < 99::AID-JBM12 > 3.0.CO;2-E.
[2] Lawrence J, Hao L, Chew HR. On the correlation between Nd:YAG laser-induced wettability characteristics modification and osteoblast cell bioactivity on a titanium alloy. Surf Coatings Technol 2006;200:5581–9. https://doi.org/10.1016/j.surfcoat.2005.07.107.
[3] Vorobyev AY, Guo C. Making human enamel and dentin surfaces superwetting for enhanced adhesion. Appl Phys Lett 2011;99:2009–12. https://doi.org/10.1063/1.3660579.
[4] Keshav TR, Basu S. Spreading of liquid droplets on proton exchange membrane of a direct alcohol fuel cell. Chem Eng Sci 2007;62:7515–22. https://doi.org/10.1016/j.ces.2007.08.019.
[5] Gau H, Herminghaus S, Lenz P, Lipowsky R. Liquid morphologies on structured surfaces: from microchannels to microchips. Science (80-) 1999;283:46–9. https://doi.org/10.1126/science.283.5398.46.
[6] Khanna R, Nigam KDP. Partial wetting in porous catalysts: wettability and wetting efficiency. Chem Eng Sci 2002;57:3401–5. https://doi.org/10.1016/S0009-2509(02)00211-7.
[7] Eick JD, Johnson LN, Fromer JR, Good RJ, Neumann AW. Surface Topography: Its Influence on Wetting and Adhesion in a Dental Adhesive System. J Dent Res 1972;51:780–8. https://doi.org/10.1177/00220345720510031401.
[8] Wenzel RN. Resistance of solid surfaces to wetting by water. Ind Eng Chem 1936;28:988–94. https://doi.org/10.1021/ie50320a024.
[9] B D Cassie BA, Baxter S. Wettability of porous surfaces. Trans Faraday Soc 1944;40:546–51. https://doi.org/10.1039/TF9444000546.
[10] Bico J, Tordeux C, Quere D. Rough wetting. Eur Lett 2001;55:214–20. https://doi.org/10.1209/epl/i2001-00402-x.
[11] McHale G, Shirtcliffe NJ, Aqil S, Perry CC, Newton MI. Topography driven spreading. Phys Rev Lett 2004;93. https://doi.org/10.1103/PhysRevLett.93.036102. 036102–1.
[12] Courbin L, Denieul E, Dressaire E, Roper M, Ajdari A, Stone HA. Imbibition by polygonal spreading on microdecorated surfaces. Nat Mater 2007;6:661–4. https://doi.org/10.1038/nmat1978.
[13] Woodward I, Schofield WCE, Roucoules V, Badyal JPS. Super-hydrophobic surfaces produced by plasma fluorination of polybutadiene films. Langmuir 2003;19:3432–8. https://doi.org/10.1021/la020427e.
[14] Wang Q, Zhang B, Qu M, Zhang J, He D. Fabrication of superhydrophobic surfaces on engineering material surfaces with stearic acid. Appl Surf Sci 2008;254:2009–12. https://doi.org/10.1016/j.egypro.2013.06.080.
[15] Martines E, Seunarine K, Morgan H, Gadegaard N, Wilkinson CDW, Riehle MO. Superhydrophobicity and superhydrophilicity of regular nanopatterns. Nano Lett 2005;5:2097–103. https://doi.org/10.1021/nl051435t.
[16] Baldacchini T, Carey JE, Zhou M, Mazur E. Superhydrophobic surfaces prepared by microstructuring of silicon using a femtosecond laser. Langmuir 2006;22:4917–9. https://doi.org/10.1021/la053374k.
[17] Zorba V, Persano L, Pisignano D, Athanassiou A, Stratakis E, Cingolani R, et al. Making silicon hydrophobic: Wettability control by two-lengthscale simultaneous patterning with femtosecond laser irradiation. Nanotechnology 2006;17:3234–8. https://doi.org/10.1088/0957-4484/17/13/026.
[18] Kietzig AM, Hatzikiriakos SG, Englezos P. Patterned superhydrophobic metallic surfaces. Langmuir 2009;25:4821–7. https://doi.org/10.1021/la8037582.
[19] Vorobyev AY, Guo C. Metal pumps liquid uphill. Appl Phys Lett 2009:94. https://doi.org/10.1063/1.3117237.
[20] Cunha A, Serro AP, Oliveira V, Almeida A, Vilar R, Durrieu MC. Wetting behaviour of femtosecond laser textured Ti-6Al-4V surfaces. Appl Surf Sci 2013;265:688–96. https://doi.org/10.1016/j.apsusc.2012.11.085.
[21] Li B, Li H, Huang L, Ren N, Kong X. Femtosecond pulsed laser textured titanium surfaces with stable superhydrophilicity and superhydrophobicity. Appl Surf Sci 2016;389:585–93. https://doi.org/10.1016/j.apsusc.2016.07.137.
[22] Tian Y, Jiang L. Wetting: Intrinsically robust hydrophobicity. Nat Mater 2013;12:291–2. https://doi.org/10.1038/nmat3610.
[23] Bizi-Bandoki P, Valette S, Audouard E, Benayoun S. Time dependency of the hydrophilicity and hydrophobicity of metallic alloys subjected to femtosecond laser

irradiations. Appl Surf Sci 2013;273:399–407. https://doi.org/10.1016/j.apsusc.2013.02.054.
[24] Long J, Zhong M, Zhang H, Fan P. Superhydrophilicity to superhydrophobicity transition of picosecond laser microstructured aluminum in ambient air. J Colloid Interface Sci 2015;441:1–9. https://doi.org/10.1016/j.jcis.2014.11.015.
[25] Samanta A, Wang Q, Shaw SK, Ding H. Roles of chemistry modification for laser textured metal alloys to achieve extreme surface wetting behaviors. Mater Des 2020. Under Review.
[26] Vadali M, Ma C, Duffie NA, Li X, Pfefferkorn FE. Pulsed laser micro polishing: surface prediction model. SME J Manuf Process 2012;14:307–15. https://doi.org/10.1016/j.jmapro.2012.03.001.
[27] Vorobyev AY, Guo C. Water sprints uphill on glass. J Appl Phys 2010;108:10–4. https://doi.org/10.1063/1.3511431.
[28] Vorobyev AY, Guo C. Laser turns silicon superwicking. Opt Express 2010;18:6455–60. https://doi.org/10.1364/OE.18.006455.
[29] Demir AG, Previtali B, Bestetti M. Microvalve actuation with wettability conversion through darkness/UV application. J Micromech Microeng 2011:21. https://doi.org/10.1088/0960-1317/21/2/025019.
[30] Ding H, Wang Q, Samanta A, Shen N. Nanosecond laser-based high-throughput surface nano-structuring (nHSN) process. US20190054571A1. 2019.
[31] Wang Q, Samanta A, Shaw SK, Hu H, Ding H. Nanosecond laser-based high-throughput surface nanostructuring (nHSN). Appl Surf Sci 2020;507:145136https://doi.org/10.1016/j.apsusc.2004.11.001.
[32] Wang Q, Samanta A, Toor F, Shaw S, Ding H. Colorizing Ti-6Al-4V Surface via High-Throughput Laser Surface Nanostructuring. J Manuf Process 2019;43:70–5. https://doi.org/10.1016/j.jmapro.2019.03.050. Elsevier.
[33] Samanta A, Wang Q, Shaw SK, Ding H. Nanostructuring of laser textured surface to achieve superhydrophobicity on engineering metal surface. J Laser Appl 2019;31:022515https://doi.org/10.2351/1.5096148.
[34] Samanta A, Huang W, Chaudhry H, Wang Q, Shaw SK, Ding H. Design of chemical surface treatment for laser textured metal alloy to achieve extreme wetting behavior. ACS Appl Mater Interfaces 2020. Under Review.
[35] Lee J, Suh Y, Dubey PP, Barako MT, Won Y. Capillary wicking in hierarchically textured copper nanowire arrays. ACS Appl Mater Interfaces 2019;11:1546–54. https://doi.org/10.1021/acsami.8b14955.
[36] O'Gara JE, Alden BA, Gendreau CA, Iraneta PC, Walter TH. Dependence of cyano bonded phase hydrolytic stability on ligand structure and solution pH. J Chromatogr A 2000;893:245–51. https://doi.org/10.1016/S0021-9673(00)00696-8.
[37] Horcajada P, Rámila A, Férey G, Vallet-Regí M. Influence of superficial organic modification of MCM-41 matrices on drug delivery rate. Solid State Sci 2006;8:1243–9. https://doi.org/10.1016/j.solidstatesciences.2006.04.016.
[38] Liu N, Yao Y, Cha JJ, McDowell MT, Han Y, Cui Y. Functionalization of silicon nanowire surfaces with metal-organic frameworks. Nano Res 2012;5:109–16. https://doi.org/10.1007/s12274-011-0190-1.
[39] Raphaël E. Capillary rise of a wetting fluid in a semi-circular groove. J Phys 1989;50:485–91. https://doi.org/10.1051/jphys:01989005004048500.
[40] Rye RR, Mann JA, Yost FG. The flow of liquids in surface grooves. Langmuir 1996;12:555–65. https://doi.org/10.1021/la9500989.
[41] Stange M, Dreyer ME, Rath HJ. Capillary driven flow in circular cylindrical tubes. Phys Fluids 2003;15:2587–601. https://doi.org/10.1063/1.1596913.
[42] Fisher LR, Lark PD. An experimental study of the washburn equation for liquid flow in very fine capillaries. J Colloid Interface Sci 1979;69:486–92. https://doi.org/10.1016/0021-9797(79)90138-3.